AIAA JOURNAL
Vol. 43, No. 8, August 2005

# Passive Control of Plume Interference on Slender Axisymmetric Bodies

Young-Ki Lee,[*] Srinivasan Raghunathan,[†] and Emmanuel Benard[‡]
*Queen's University of Belfast, Belfast, Northern Ireland BT9 SAG, United Kingdom*

**The physics of the plume-induced shock and separation, particularly at high plume to exit pressure ratios with and without shock–turbulent boundary-layer control methods, were studied using computational techniques. Mass-averaged Navier–Stokes equations with a two-equation turbulence model were solved by using a fully implicit finite volume scheme and time-marching algorithm. The control methodologies for shock interactions included a porous tail and a porous extension attached at the nozzle exit or trailing edge. The porous tail produced a weaker shock and fixed the shock position on the control surface. The effect of the porous extension on shock interactions was mainly to restrain the plume from strongly underexpanding during a change in flight conditions. These techniques could give an additional dimension to the design and control of supersonic missiles.**

## Nomenclature

$\mathbf{A}$ = area vector
$a$ = sound speed
$C_p$ = specific heat at constant pressure
$D$ = diameter of missile
$E$ = total energy per unit mass
$\mathbf{F}$ = inviscid flux vector
$\mathbf{G}$ = viscous flux vector
$H$ = total enthalpy per unit mass
$k$ = turbulent kinetic energy
$l_p$ = length of porous wall
$M, M_t$ = Mach number, turbulent Mach number
$p$ = pressure, Pa
$\mathbf{Q}$ = dependent vector of primitive variables
$\mathbf{q}$ = heat flux vector
$U, U_r$ = velocity magnitude, reference velocity
$V$ = control volume
$\mathbf{v}$ = velocity vector, $v_x\hat{i} + v_y\hat{j} + v_z\hat{k}$, where, $v_x$, $v_y$ and $v_z$ are velocity components in Cartesian coordinates
$x_s$ = position of plume-induced shock
$\mathbf{\Gamma}$ = preconditioning matrix
$\gamma$ = ratio of specific heats
$\varepsilon$ = turbulent dissipation rate
$\mu_t$ = turbulent viscosity
$\rho, \rho_t$ = density, derivative of density on temperature at constant pressure
$\tau_{ij}$ = viscous stress tensor

### *Subscripts*

$a$ = atmospheric state
$c$ = combustion chamber
$e$ = exit of supersonic nozzle
$0$ = total state
$\infty$ = freestream

## Introduction

SUPERSONIC speeds are the rule for most modern missiles, which require a very high thrust level within a limited cross-sectional area. The aerodynamic designs in recent years, therefore, have focussed on understanding several problems associated with the plume expansion at high speeds and altitudes. These configurations generally have a highly underexpanded jet plume[1,2] downstream of the exhaust nozzle exit, leading to considerable interactions between the exhaust plume and freestream near the tail of missile bodies. The boundary-layer separation[3,4] and pitching and yawing moments that result from the interactions can have significant effects on missile stability and control.[5,6]

Plume interference[7] is an extremely complicated phenomenon, consisting of plume-induced boundary-layer separation, separated shear layers, multiple shockwaves, and interactions as shown in Fig. 1. As is the case for a supersonic shock–boundary-layer interaction with a separation bubble, the wave system consists of a $\lambda$-shaped shock with expansion waves inside the shock foot. The shock-induced separation near the missile tail, where fins are normally located, can have an adverse effect on control. The flow characteristics are inherently nonlinear and severely unstable during the flight at its normal speed as well as at launching. In particular, unsteady higher static pressures in the separation region near the trailing edge can cause unbalanced forces on the missile. The control of shock-induced separation is, therefore, one of the most important considerations for the effective design of powered missiles and flight vehicles.

Most of the knowledge base on plume–freestream interactions on afterbody surfaces of powered missiles is from wind-tunnel tests. Salmi,[8] Hinson and McGhee,[9] and Hinson and Falanga[10] examined the effects of underexpanded jet plumes on the static stability of missile bodies at supersonic speeds. They concluded plume interference effects could alter the pressure distribution on the aft surface of a missile body, resulting in changes in the aerodynamic forces and moments acting on it. McGhee,[11] McGhee and Martin,[12] and McGhee[13] performed experiments on the effects of jet plume-induced flow separation on several axisymmetric bodies with various forebody and afterbody geometries at supersonic speeds. Their main conclusion was that, at relatively lower freestream Mach numbers, separation regions were small and the jet pressure ratio required to induce the separation was relatively lower than when compared with the results at higher Mach numbers. Wu and Aoyama[14] and Wu et al.[15,16] investigated transonic flowfields around various bodies of revolution with and without plumes. Their investigation showed that the viscous effect on the boattailed region upstream of the plume exhaust was very significant.

A detailed understanding of plume-interference phenomena for an arbitrary missile model is indispensable to missile design.

---

Received 31 May 2003; revision received 24 November 2003; accepted for publication 24 January 2005. Copyright © 2005 by the American Institute of Aeronautics and Astronautics, Inc. All rights reserved. Copies of this paper may be made for personal or internal use, on condition that the copier pay the $10.00 per-copy fee to the Copyright Clearance Center, Inc., 222 Rosewood Drive, Danvers, MA 01923; include the code 0001-1452/05 $10.00 in correspondence with the CCC.

[*] Research Student, School of Aeronautical Engineering, David Keir Building, Stranmillis Road.

[†] Professor, School of Aeronautical Engineering, Bombardier Aerospace–Royal Academy Chair. Member AIAA.

[‡] Lecturer, School of Aeronautical Engineering.

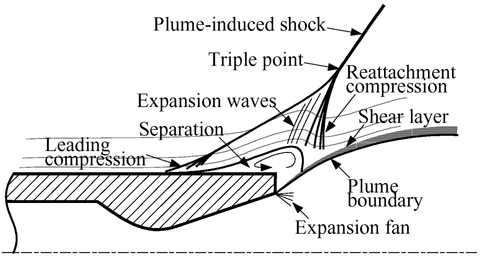

**Fig. 1 Schematic diagram of plume interference phenomena.**

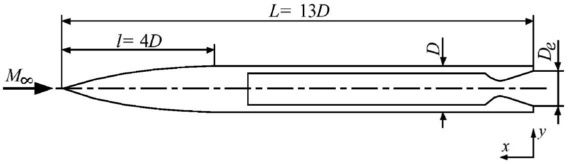

**a) Model simple**

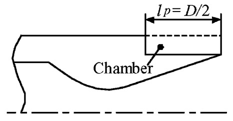

**b) Model PW**

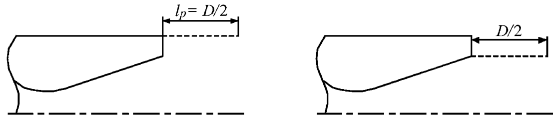

**c) Model PD** **d) Model PDE**

**Fig. 2 Testing models and afterbody configurations.**

However, because of excessive assumptions to solve complex viscous–inviscid interactions and simple pressure measurements provided through most theoretical and experimental studies to date, the current knowledge base built in this research area is not adequate to provide an overall insight into the physics involved. Computational fluid dynamics (CFD) analyses, therefore, offer a way forward for the development of such a design. Very recently, some computational work[17,18] has been done mainly on base flow problems but, to the authors' knowledge, no CFD study has been conducted for the control of plume interference phenomena.

In this research, CFD studies were conducted for missile models with a simple afterbody, porous tail, and porous extension to simulate moderately and highly underexpanded exhaust plumes mainly at supersonic speeds. A fully implicit finite volume scheme was applied to mass-averaged Navier–Stokes equations with a two-equation turbulence model, renormalization group (RNG) $k$–$\varepsilon$. The present numerical study may develop a basic understanding into the influence of the porous tail and porous extension on the plume-induced shockwave and separation, leading to the effective and efficient control of flight bodies.

## Model Configuration

Figure 2 shows the schematic diagrams of missile models tested in this CFD analysis. The present computational model can be basically represented as an ogive forebody and straight afterbody without tail fins, identified as model simple. The 13-caliber missile body for the code validation had a 4-caliber tangent ogive nose and a cylindrical afterbody diameter of 63.5 mm. A convergent–divergent nozzle, having a design Mach number of 2.7, an exit diameter of $D_e = 50.9$ mm, and a divergence angle of 20 deg, was used to acquire supersonic plumes downstream of the nozzle exit. A porous tail model with a porous wall length of $l_p = D/2$ and porosity of 0.5 was named as model PW, in which the porous wall covers a plenum chamber to produce a self-circulation by using the pressure difference before and behind a shockwave on the device. For porous extension models, model PD and PDE with the same porous wall as model PW, the porous wall was attached to the afterbody edge and nozzle exit, respectively. The afterbody models given here were tested to find an effective method of controlling the flow features that may adversely affect overall missile performance.

## Numerical Simulations

### Governing Equations

The system of mass-averaged, time-dependent Navier–Stokes equations governing the flowfields around missiles is given in conservation form. The resulting equations are expressed in integral form for an arbitrary control volume $V$ with differential surface area d$\boldsymbol{A}$:

$$\boldsymbol{\Gamma}\frac{\partial}{\partial t}\int_V \boldsymbol{Q}\,\mathrm{d}V + \oint [\boldsymbol{F}-\boldsymbol{G}]\cdot \mathrm{d}\boldsymbol{A} = 0 \tag{1}$$

where $\boldsymbol{F}$ and $\boldsymbol{G}$ are inviscid and viscous flux vectors in standard conservation form and $\boldsymbol{Q}$ is the dependent vector of primitive variables, transformed at the first step of the preconditioning treatment[19] employed to predict conserved quantities effectively. The vectors are given by

$$\boldsymbol{F} = \begin{bmatrix} \rho\boldsymbol{v} \\ \rho\boldsymbol{v}v_x + p\hat{i} \\ \rho\boldsymbol{v}v_y + p\hat{j} \\ \rho\boldsymbol{v}v_z + p\hat{k} \\ \rho\boldsymbol{v}H \end{bmatrix}, \qquad \boldsymbol{G} = \begin{bmatrix} 0 \\ \tau_{xi} \\ \tau_{yi} \\ \tau_{zi} \\ \tau_{ij}v_j + \boldsymbol{q} \end{bmatrix}, \qquad \boldsymbol{Q} = \begin{bmatrix} p \\ v_x \\ v_y \\ v_z \\ T \end{bmatrix} \tag{2}$$

In Eq. (2), the total enthalpy per unit mass $H$ is related to the total energy per unit mass $E$ by $H = E + p/\rho$, where $E$ includes both internal and kinetic energy. $\boldsymbol{\Gamma}$ is included in Eq. (1) to provide more accurate velocity and temperature gradients in viscous fluxes and pressure gradients in inviscid fluxes. The advantage of the preconditioning treatment in the calculations is that the propagation of acoustic waves in the system can be singled out.[19] This matrix is given by

$$\boldsymbol{\Gamma} = \begin{bmatrix} \theta & 0 & 0 & 0 & \rho_T \\ \theta v_x & \rho & 0 & 0 & \rho_T v_x \\ \theta v_y & 0 & \rho & 0 & \rho_T v_x \\ \theta v_z & 0 & 0 & \rho & \rho_T v_x \\ \theta H - \delta & \rho v_x & \rho v_x & \rho v_x & \rho_T H + \rho C_p \end{bmatrix} \tag{3}$$

where $\rho_T$ is the derivative of density with respect to temperature at constant pressure and $\delta = 1$ for compressible flow. The parameter $\theta$ is specified by

$$\theta = \left(1\big/U_r^2 - \rho_T/\rho C_p\right) \tag{4}$$

In Eq. (4), $U_r$ is chosen such that the eigenvalues of the system remain well conditioned with respect to the convective and diffusive timescales.

A two-equation turbulence model, RNG $k$–$\varepsilon$ (Ref. 20) modified to take into account compressibility effects, was employed to close the governing equations. The turbulent Mach number used in the dilatation term of the turbulence model is identified as $M_t = (k/a^2)^{0.5}$. The model for the turbulent viscosity $\mu_t$ is written as $\mu_t = \rho C_\mu (k^2/\varepsilon)$, where the turbulent kinetic energy $k$ and dissipation rate $\varepsilon$ are solved from the turbulent transport theory. The following model constants are used: $C_\mu = 0.0845$, $C_{1\varepsilon} = 1.42$, and $C_{2\varepsilon} = 1.68$.

### Numerical Schemes

The present investigation adopted a commercial computational code, FLUENT 5,[21] to analyze complex compressible flows around missile bodies. This CFD code has the ability to predict flowfields involving strong shock interactions with shear layers and boundary layers and is expected to provide high-quality simulations for the flowfield around a missile body with a highly underexpanded plume.

The governing equations are discretized spatially by using a fully implicit finite volume scheme, in which the physical domain is subdivided into numerical cells and the integral equations are applied to each cell. The flowfield is represented by associating a distinct value of the discretized solution vector with each control volume, which is then used to evaluate the fluxes at the cell faces. The solution vector is computed using a multidimensional linear reconstruction approach,[22] which enables higher-order accuracy to be achieved at the cell faces through a Taylor series expansion of the cell-averaged solution vector. The use of a second-order accurate scheme makes it feasible to capture the shock structure and boundary-layer flows near-wall regions, but only by using fine computational grids. With respect to temporal discretization, an explicit multistage time-stepping scheme[23] is used to discretize the time derivatives in the governing equations. Then it is assumed that time marching proceeds until a steady-state solution is reached.

To acquire accurate solutions, CFD analyses must be conducted by using a proper computational domain and grid quality in consideration of the flow features to be expected especially in missile aerodynamics. In the present computation, grid adaptation and higher-order approximation schemes were used to get more reliable results. A second-order accurate scheme was selected to capture correctly the flow features with strong pressure gradients, such as various shock structures, shear layers, and plume boundaries, and the wake flow downstream of the afterbody of missile models.

The code was validated for the missile model with a sharp edge under several test conditions with available results of past wind-tunnel tests.[24] Some representative results of the code validation will be discussed in the results section.

### Computational Grids

Figure 3a shows the detailed layout of the grids near the afterbody edge and exhaust jet region. The computational domain was chosen to take into account the large plume expansion at high pressure ratios. The shock waves and mixing layers are very thin, and the convergence of solutions strongly depends on plume dimensions and locations of shock waves inside the plume and on the afterbody. Therefore, grids were clustered in regions with large gradients, such as shock waves, shear layers, and boundary layers, to provide more accurate predictions of the flowfield. For some cases with a highly underexpanded plume, grid adaptation was applied to shear layers, plume boundaries, and discontinuities in the region with coarse grids.

The fineness of computational grids required to obtain grid-independent solutions was first examined for some of the flowfields under consideration. Figure 3b shows a typical result of grid-convergence tests for a flight condition of $p_c/p_a = 341.8$ and $M_\infty = 2.0$, which produces the largest plume dimensions among tested cases at supersonic speeds. The continuity residuals given here are converged values for each grid size when the mass imbalance for inlet, outlet, and freestream boundaries became approximately unchangeable. For the several testing grid systems, Fig. 3c shows a grid fineness test result with the velocity profiles acquired at the afterbody edge. When about 140,000 nodes were used, the solution for the given flight condition was considered correct because there was no change observed not only in the residual but also in the velocity profile with a further increase in the grid size. The grid fineness for the models with a porous tail or porous extension was judged by using the same approach, and about 150,000 nodes were fine enough for all cases tested.

### Boundary Conditions and Analysis

Axisymmetric plume flowfields were initiated from highly compressed air in the combustion chamber and expanded to supersonic external flowfields through the converging–diverging nozzle. The expansion occurred according to the plume pressure ratio, which is the ratio of chamber total pressure $p_c$ to atmospheric pressure $p_a$. The mass flow boundary condition was applied to the combustion chamber inlet, where $p_c$ was adjusted to achieve the velocity needed to provide the prescribed mass flux at the boundary. The pressure far-field condition was used for the half-parabolic boundary enclosing the model to specify freestream conditions at infinity with the freestream Mach number and static conditions. This condition uses the Riemann invariants to determine the flow variables at the boundary. The pressure outlet boundary condition was applied to the vertical boundary at the end of the computational domain with only static pressure specified.

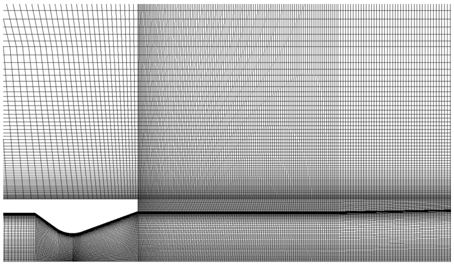

a) Structural grids near the simple afterbody

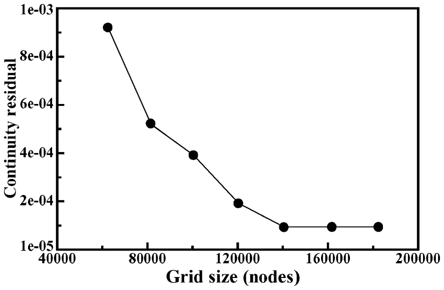

b) Grid convergence with continuity residual

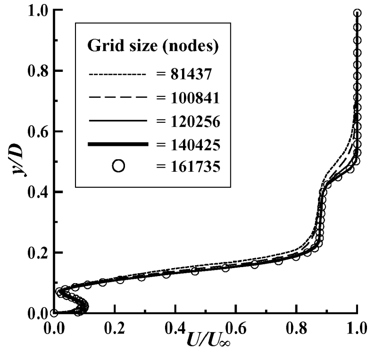

c) Grid fineness tests with velocity profiles

**Fig. 3 Grid system and convergence at $p_c/p_a = 341.8$ and $M_\infty = 2.0$.**

The main parameters to characterize plume–freestream interactions were the plume pressure ratio $p_c/p_a$ and freestream Mach number $M_\infty$ in the ranges of 50–350 and 1.2–3.0, respectively. These ranges covered moderately to highly underexpanded plumes embedded in supersonic external flows. For simplicity, the effect of total temperature was not taken into account. Freestream pressure and temperature were assumed to be constant with values of 1 atm and 288.15 K, respectively. With a proper grid size chosen by using the approach explained through Fig. 3, basically, solutions were considered converged when the residuals for all equations drop by three orders of magnitude, typically $10^{-4}$ as shown in Fig. 3b, with the mass imbalance check for flow inlet and outlet boundaries.

## Results

### Code Validation

The validations of the present computational code for $M_\infty = 0.9$ and 1.2 are given in Fig. 4. Static pressure distributions were measured from the end of the afterbody surface toward upstream with distance $x$. (See the schematic diagram in Fig. 4.) Here, $x$ and local static pressure along the missile surface were normalized by the model diameter $D$ and atmospheric pressure $p_a$, respectively. All pressure distributions in this paper follow this convention.

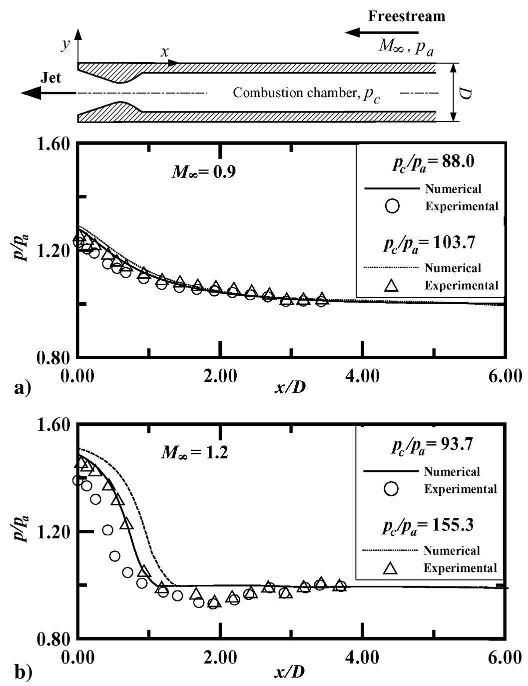

Fig. 4 Validation of the computational code with wind-tunnel tests.

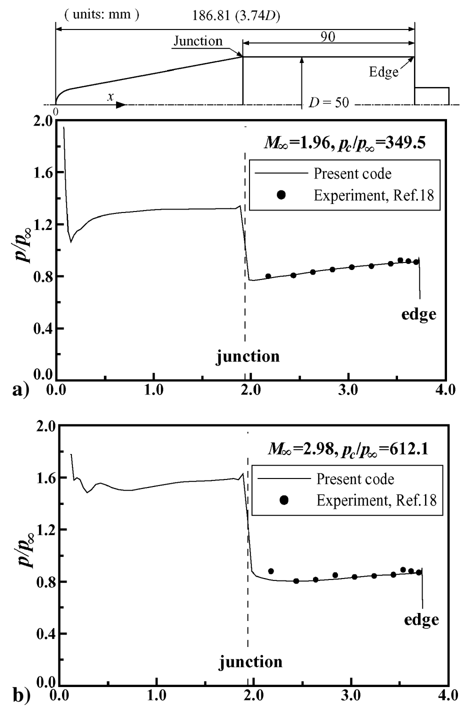

Fig. 5 Experimental and numerical wall pressure distributions along a cone–cylinder model at supersonic speeds.

The results show reasonable agreement with the limited available pressure measurements taken from a past wind-tunnel experiment.[24] At the lower Mach number of 0.9, the present code gave better predictions for the pressure rise before the plume expansion. However, with a stronger pressure rise at $M_\infty = 1.2$, the differences for the compression region become larger, and these could be attributed to the inability of the CFD code to estimate accurately a sharp pressure rise in this region. The fluctuations in the experimental pressure values upstream of the sharp pressure rise at $M_\infty = 1.2$ can result from support strut–plume interference and blockage effects in the wind-tunnel tests.

Figures 5 and 6 present the validation results for supersonic flows over a blunt cone–cylinder model with the jet Mach number about 4.0, taken from Ref. 18, which was selected because no experimental data for the supersonic flowfields over the present missile model are given in the data sets of Ref. 24. The geometric details are schematically shown in Fig. 5. Two testing conditions, $p_c/p_\infty = 349.5$ and 612.1 at $M_\infty = 1.96$ and 2.98, respectively, were selected to validate the code for strong plume interference at supersonic speeds. In the computational domain, the influence of strut and wind-tunnel wall on the flowfield was not taken into account.

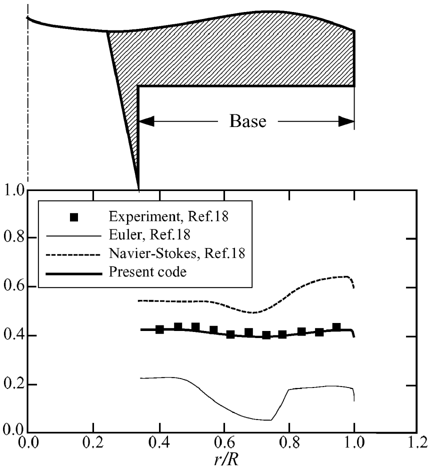

a) $M_\infty = 1.96$ and $p_c/p_\infty = 349.5$

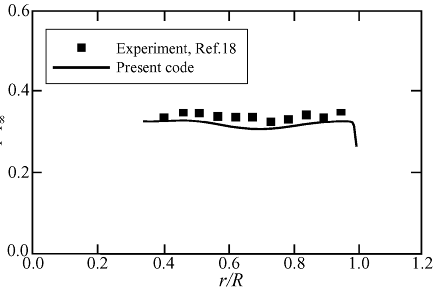

b) $M_\infty = 2.98$ and $p_c/p_\infty = 612.1$

Fig. 6 Experimental and numerical base pressure distributions.

When the surface pressure distributions estimated by the present CFD code and the experiment are compared (Fig. 5), the pressure data were predicted from the nose to the edge of the model in the CFD analysis and from the junction of cone and afterbody toward the downstream in the experiment. Good agreement between the predicted and measured pressure values is observed at both Mach numbers. The slight fluctuations in measured pressure values shown in Figs. 5a and 5b can be attributed to the irregularity of the pressure taps[18] and the effects of the wind-tunnel wall and strut in the experiment as shown in Fig. 4. Because wave generation becomes stronger with the higher Mach number and higher pressure ratio, the disagreement increases because of a stronger wave–model interaction.

With regard to base pressure distributions, the predictions by the present code were compared with Euler and Navier–Stokes calculations without turbulence modeling[18] and experimental data[18] (Fig. 6). Base pressure values and radial distance $r$ were normalized by the freestream pressure $p_\infty$ and the radius of the afterbody $R$, respectively. It can be observed that, for $M_\infty = 1.96$ and $p_c/p_\infty = 349.5$, the present code gave good predictions quantitatively and qualitatively, whereas the Euler and Navier–Stokes simulations significantly underpredicted or overpredicted pressure values (Fig. 6a). Also for the higher Mach number and higher pressure ratio, the present CFD result shows reasonable agreement with the experimentally measured pressure values (Fig. 6b). Therefore, it is considered that the implemented turbulence model in the present CFD code is appropriate to simulate a flowfield in such a viscous-dominant region.

### Supersonic Flows over Model Simple

According to a previous study,[25] for the present missile configuration (model simple), unless the missile speed exceeded the sonic Mach number, approaching flow toward a highly underexpanded plume would be always compressed by a series of compression waves because no locally supersonic region existed along the straight afterbody. For this type of missile model, therefore, the plume-induced shock and separation are the interference features peculiar to supersonic flows. The computational results regarding model simple focus on the behavior of the detrimental phenomena according to changes in flight conditions at supersonic speeds.

The Mach number contours for a fixed pressure ratio of 170.9 in Fig. 7 show the influence of the freestream Mach number on the flowfield around the model with a sharp corner. At $M_\infty = 1.2$ (Fig. 7a), the plume-induced shock is represented as an oblique shock wave for the leading compression, which occurs at a far upstream location on the afterbody surface. As $M_\infty$ becomes 1.5 (Fig. 7b), the leading compression waves before boundary-layer separation and reattachment compression waves coalesce into the plume-induced shock wave, consequently forming a λ-shaped reflection. While $M_\infty$ increases, the higher dynamic energy of freestream may more strongly restrict the expansion of the plume. Therefore, it can be observed that plume dimensions are reduced, the shock cell structure moves upstream, and the plume-induced shock moves downstream. Also note that, at $M_\infty = 3.0$ (Fig. 7d), the λ-shaped pattern of the shock changes into a single oblique shock with reduced boundary-layer separation. This implies, during an acceleration of supersonic missiles up to its normal speed, there can be a significant change in the interaction features near the base, consequently, making the flight very unstable.

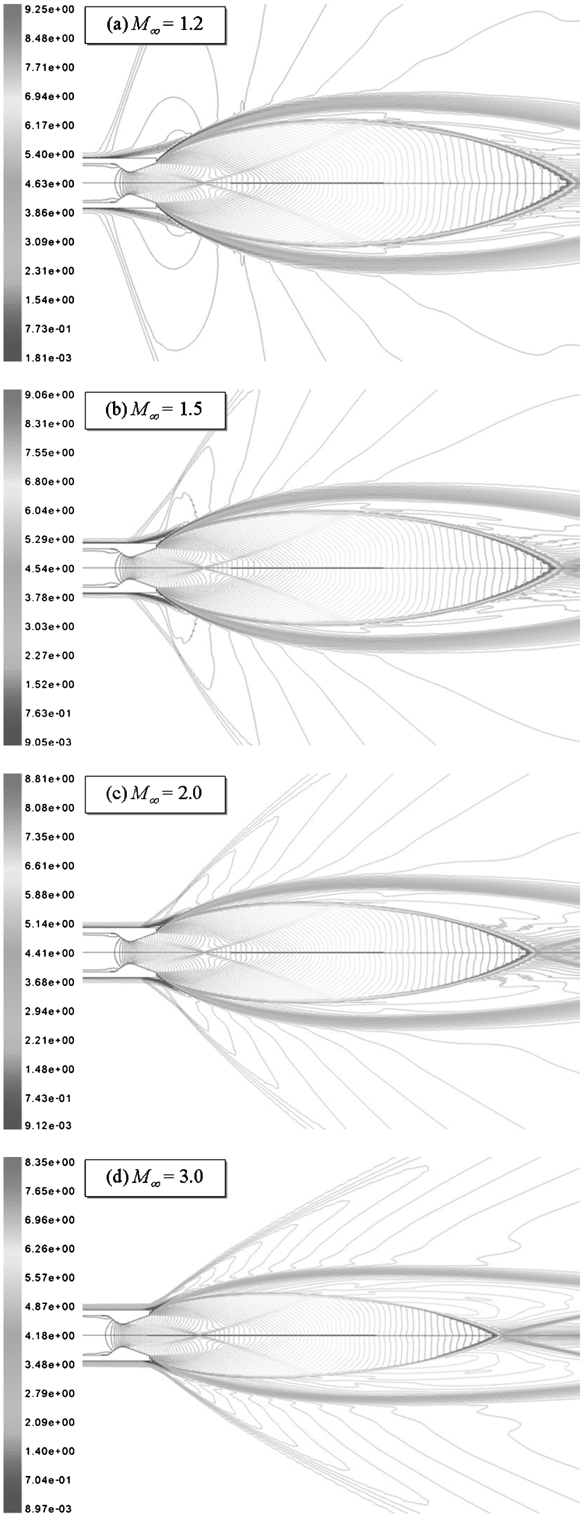

**Fig. 7 Mach number contours around model simple for various freestream Mach numbers at $p_c/p_a = 170.9$.**

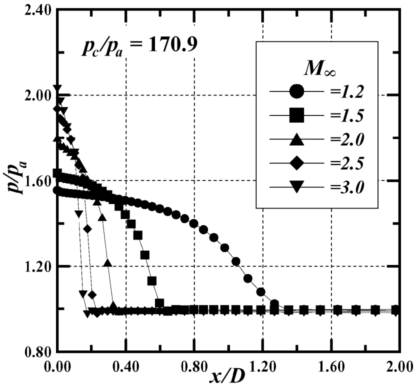

**Fig. 8 Effect of freestream Mach number on wall pressure distributions at $p_c/p_a = 170.9$.**

The static pressure distributions near the tail of model simple at $p_c/p_a = 170.9$ in Fig. 8 show shock locations and the spread of the shock system for Mach 1.2 to 3.0. With an increase in the freestream Mach number, the shock becomes stronger, the extent of shock interaction is reduced, and the shock moves downstream, consequently approaching the afterbody edge of the model. A further increase in the flight Mach number, therefore, would give an insignificant shock movement to the downstream.

Figures 9 and 10 show, for a fixed freestream Mach number of 2.0, the effect of the plume pressure ratio on the overall flow features and pressure distributions near the tail of model simple (sharp corner). As the plume pressure ratio increases, there is a stronger expansion through the nozzle so that the plume dimensions in angle and length are significantly increased. This should result in the upstream movement of both plume-induced shock and boundary-layer separation near the afterbody edge. Furthermore, as observed from the pressure distributions (Fig. 10), an increase in the plume pressure ratio increases the shock strength and length of the shock interaction region.

The results of fundamental flow features examined by using the simple missile model with a sharp edge showed that both changes in the plume pressure ratio and freestream Mach number led to severe influences on plume interference phenomena. In real flight, a strong shock and separation on afterbody surfaces can introduce several adverse effects on the flight stability and control, such as a significant shock load, buffeting, unstable pitching and yawing moments, and large pressure drag. Therefore, controlling the plume interference can be an essential consideration into the design of supersonic powered missiles with high thrust levels.

### Effects of a Porous Tail on Plume Interference

A passive control method of plume interference here involves placing a porous wall beneath shock–boundary-layer interaction (SBLI) to allow high-pressure backflows near plumes to pass through a chamber, covered with a perforated surface, into low-pressure regions before the plume-induced shock. A porous surface length of $D/2$ was chosen to evaluate how it works according

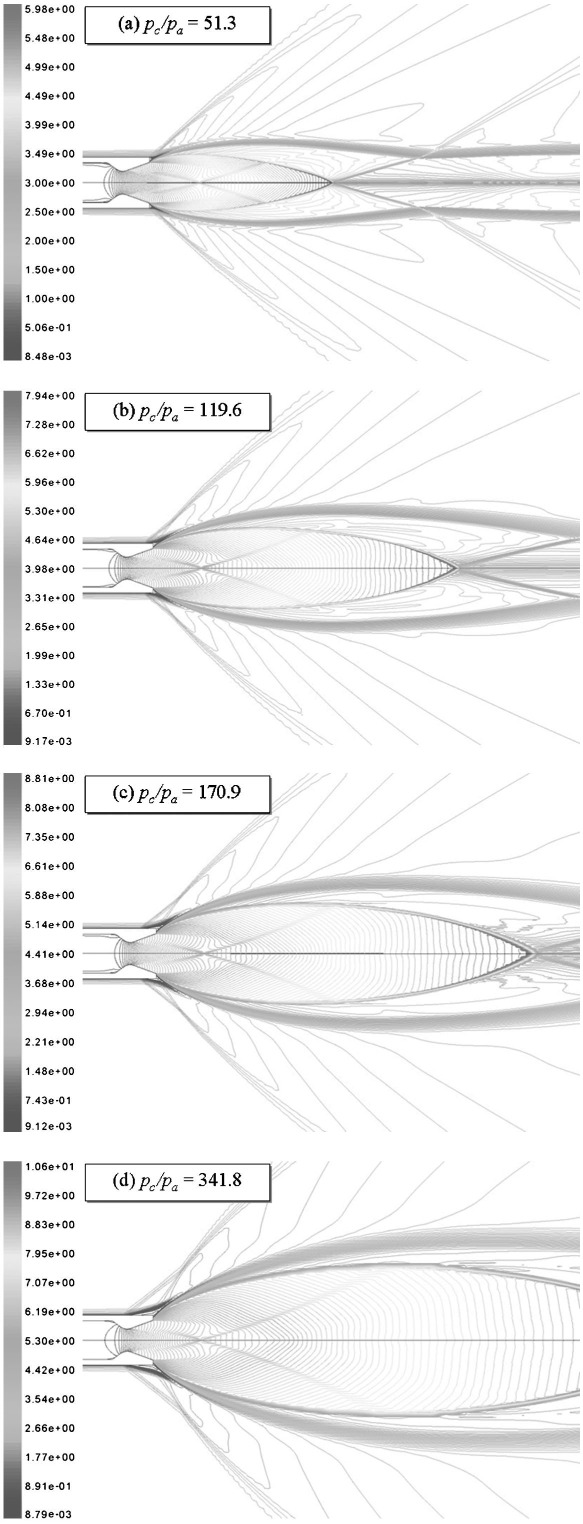

**Fig. 9 Mach number contours around model simple for various plume pressure ratios at $M_\infty = 2.0$.**

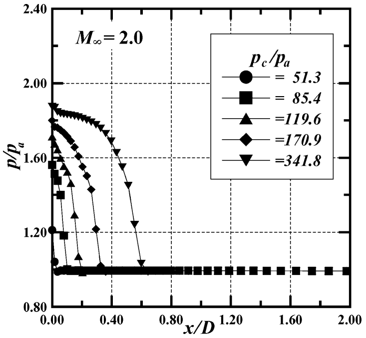

**Fig. 10 Effect of the plume pressure ratio on wall pressure distributions at $M_\infty = 2.0$.**

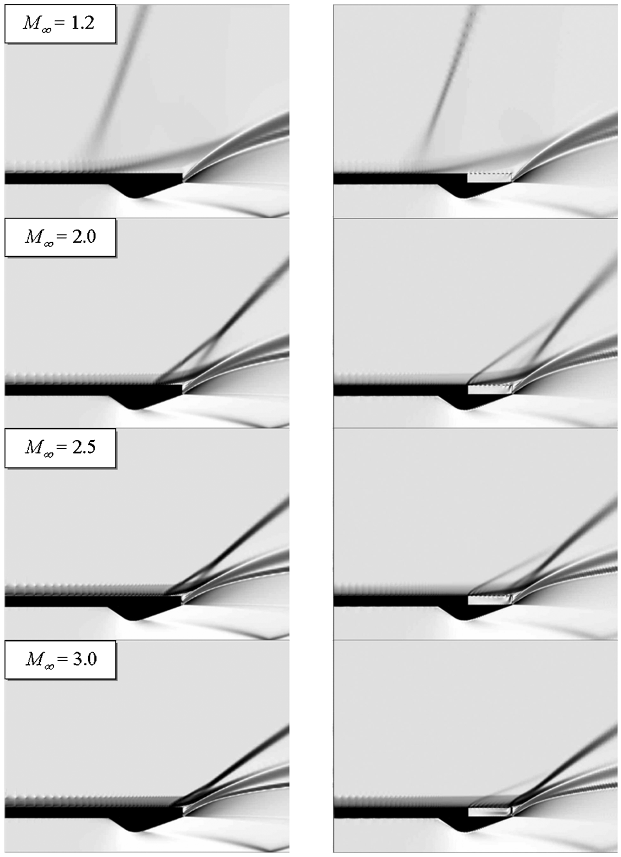

**a) Model simple** **b) Model PW**

**Fig. 11 Computed schlieren images for models simple and PW at $p_c/p_a = 170.9$.**

to shock positions inside and outside the range of the device, $x = 0–D/2$, which was the range with intense SBLI for most cases tested.

At a fixed pressure ratio of 170.9, Fig. 11 shows computed schlieren images for models simple and PW with changes in the freestream Mach number. When a main shock is located at a position of control on model simple, the wave production through the device on model PW leads to a weaker λ shock system. In this situation, leading compression waves form a weak shock in front of the device, as was observed in transonic flows,[26] which means there are strong wave interactions with the main shock. When the main shock is generated at a far upstream location (at $M_\infty = 1.2$), however, the passive device is completely embedded in the separation region and so did not function properly.

The static pressure distributions at $p_c/p_a = 170.9$ in Fig. 12 show that a porous tail affects SBLI features significantly as the freestream Mach number changes. The porous wall is positioned in the shaded range, $x/D = 0–0.5$, as shown in Fig. 12a. At a low Mach number of 1.5, a condition that the shock originally occurs upstream of the porous wall range, the device produces very weak waves so that the control effect is insignificant. For the given pressure ratio, as the shock moves into the range of the porous tail with increased Mach numbers (Figs. 12b and 12c), shock strength is considerably reduced because of stronger wave interactions. This implies that the use of a porous tail near the fin location can alleviate the shock loading on fins. In addition, the leading shock is fixed at a position slightly upstream of the control device. These can be contributed to the succeeding waves produced on the thickened boundary layer by self-injections through the porous wall and, consequently, can lead to easier shock control.

At a fixed Mach number of 2.0, computed schlieren images in Fig. 13 and static pressure distributions in Fig. 14 show the

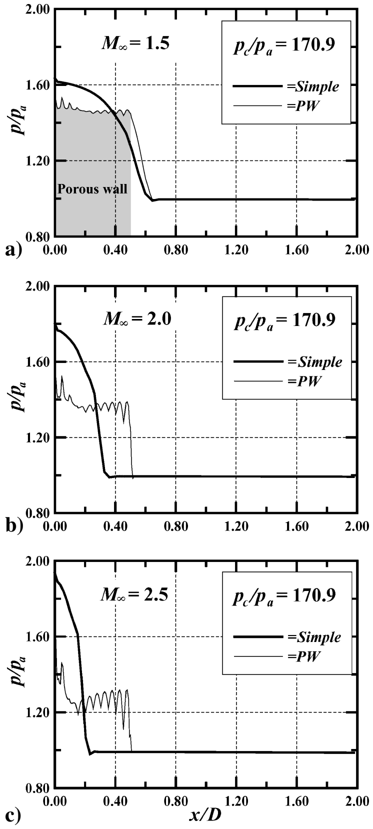

**Fig. 12 Effect of a porous tail on pressure distributions with changes in freestream Mach number at $p_c/p_a = 170.9$.**

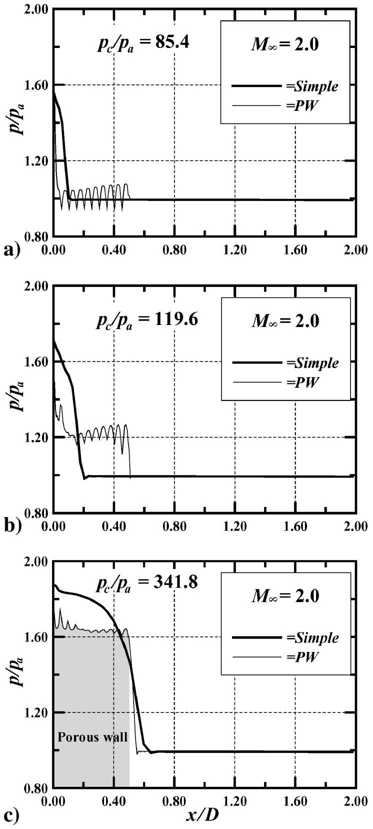

**Fig. 14 Effect of a porous tail on pressure distributions with changes in plume pressure ratio at $M_\infty = 2.0$.**

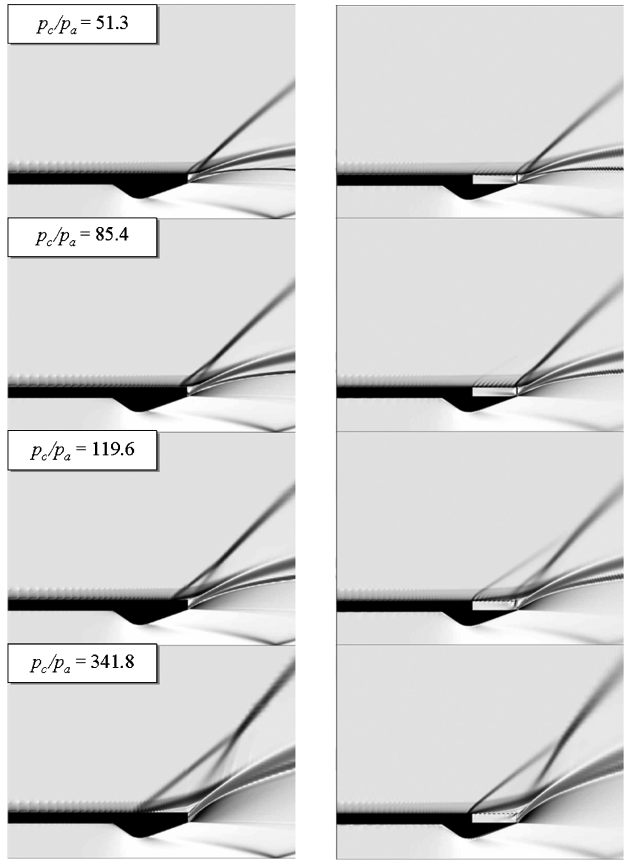

**a) Model simple** **b) Model PW**

**Fig. 13 Computed schlieren images for models simple and PW at $M_\infty = 2.0$.**

effect of a porous tail on plume-induced flow features with changes in the plume pressure ratio. For relatively low pressure ratios of $p_c/p_a \leq 85.4$ (Fig. 13), shock control is not effective, although there are strong waves produced on the device (also Fig. 14a). This can be attributed to the main shock locations near the afterbody edge, making the interactions with the waves by the device weaker. Therefore, no significant improvement in the reduction of shock strength is observed at such low pressure ratios. With a further increase in the pressure ratio, at $p_c/p_a = 119.6$, the shock moves toward the region where circulating flows are emitted through the porous wall, and therefore, the wave interactions become stronger, as shown at $M_\infty \geq 2.0$ in Fig. 11. When the shock occurs upstream of the device at a high pressure ratio of 341.8, due to weaker wave interactions, the shock slightly moves downstream, but the reduction of shock strength is relatively less significant when compared with that shown in Fig. 14b.

### Control of Plume Interference by a Porous Extension

It has been found that the main source of boundary-layer separation ensuing the plume-induced shock was significantly large plume dimensions, which are inevitable for modern supersonic missiles, relative to the missile diameter. Another type of porous wall, named here porous extension, is attached to the afterbody edge (model PD) or nozzle exit (model PDE), parallel to the afterbody to reduce plume dimensions without a loss of thrust. The models were tested for Mach numbers from 1.2 to 3.0 at a fixed pressure ratio of 170.9, which is a typical value representing large underexpansion with the present missile configuration.

In Fig. 15, the Mach number contours for models simple, PD, and PDE at $p_c/p_a = 170.9$ and $M_\infty = 1.5$ show the effects of porous extensions on the plume interference near the tail of the models. Both porous extension models present reduced plume dimensions in the radial direction with no significant change in jet cell length in comparison with model simple. The control device, however, yields different performance for control of the plume-induced shock according to device locations. In the presence of a porous extension,

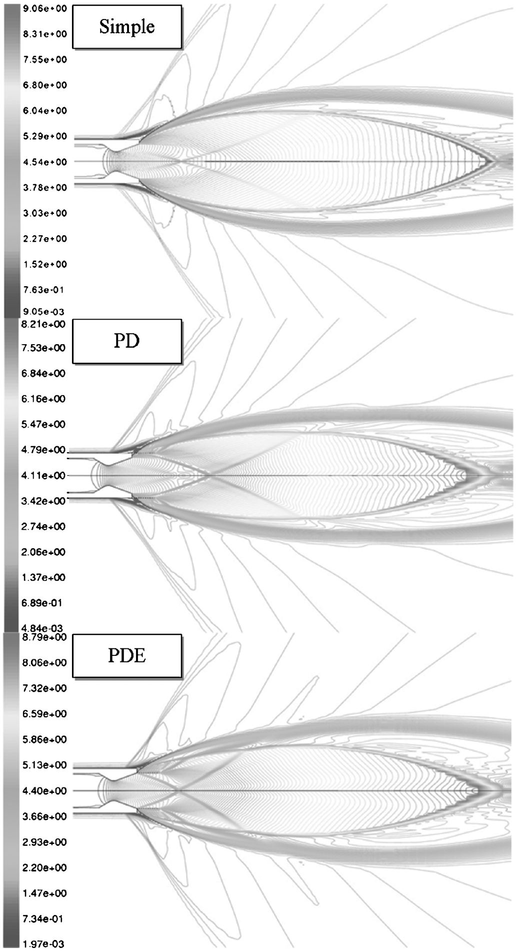

**Fig. 15 Effect of porous extension on flowfield near trailing edge at $p_c/p_a = 170.9$ and $M_\infty = 1.5$.**

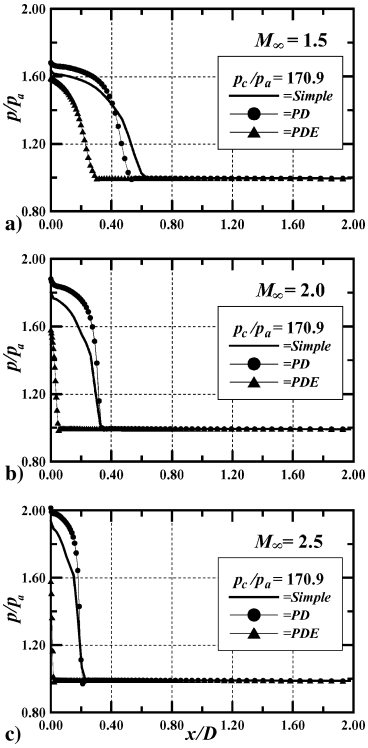

**Fig. 16 Effect of porous extension on pressure distributions at $p_c/p_a = 170.9$.**

the λ-shaped shock observed on the afterbody of model simple becomes nearly a single oblique shock due to a reduced angle of the compression corner formed by plume boundaries. However, note that shock locations are strongly dependent on the position of the porous extension.

At $M_\infty = 1.5$, 2.0, and 2.5, the static pressure distributions for a fixed $p_c/p_a$ of 170.9 given in Fig. 16 shows changes in shock locations and strength with porous extension models. For model PD, when compared with model simple, there is no significant enhancement in shock movement and the pressure rise behind the shock is increased for all flight speeds, whereas model PDE gives downstream locations of the shock with considerably reduced strength. The location of the porous extension, therefore, must be chosen carefully, and the nozzle exit would be a good recommendation. The poor control performance for model PD explained in Figs. 15 and 16 can be understood more clearly with the following results.

At $M_\infty = 2.0$ and $p_c/p_a = 170.9$, Fig. 17 presents computed schlieren images to describe the detailed flowfields in the control range for model simple and porous extension models. On the afterbody of model simple, a clear λ-shaped reflection of the shock system is generated by separation and reattachment of the boundary layer approaching the plume expansion. When a porous extension is attached to the nozzle exit (model PDE), the shock moves to the tailing edge with a considerably reduced angle of plume expansion, flattening the curvature of the compression corner. The reduced pressure rise across the shock observed in Fig. 16b can be attributed to the wave interactions between the leading shock and succeeding compression waves along the flattened plume boundary rather than a relatively stronger single reattachment shock. On the other hand, when the device is attached to the afterbody edge (model PD), no distinct downstream shock movement is observed, although plume dimensions are smaller than those of model simple. Observe that model PD produces intense flows emitted from the perforated wall, making the back flow in the separation region very strong and thus resulting in poor control performance.

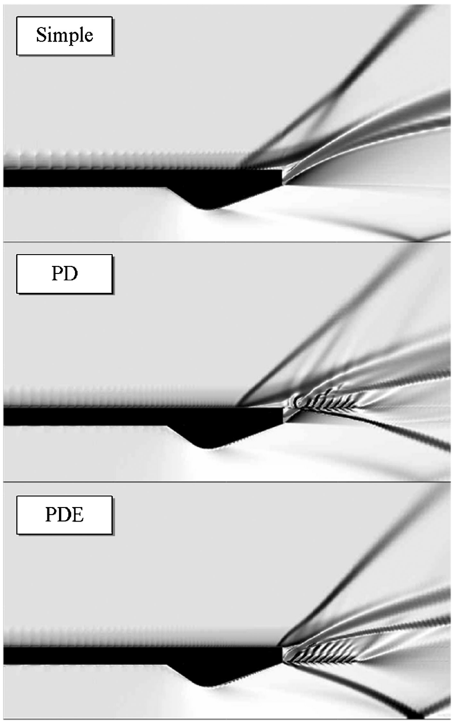

**Fig. 17 Computed schlieren images for models simple, PD, and PDE at $M_\infty = 2.0$ and $p_c/p_a = 170.9$.**

Comparison of shock positions in Fig. 18 summarizes the effectiveness of each method on shock control in terms of shock movements. The porous tail model (model PW) functions in a way to fix shock locations just in front of the device, placed from $x/D = 0.5$

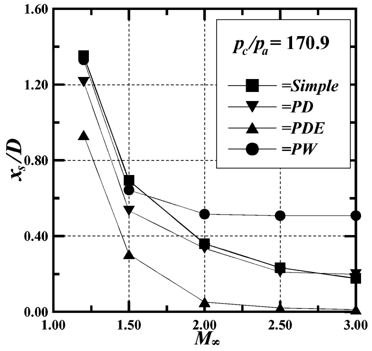

**Fig. 18 Effects of porous walls on shock positions with changes in freestream Mach number.**

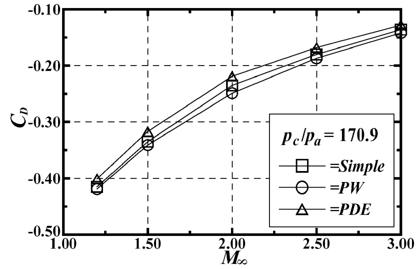

**Fig. 19 Total drag at supersonic speeds.**

to 0, at relatively high Mach numbers of $M_\infty = 2.0$. Consequently, the total movement of the shock $\Delta x_s/D$ for the speed range tested reduces by about 0.36 calibers due to the succeeding waves produced by self-circulation through the device, interacting with the main shock system. With an improper position of a porous expansion, such as model PD, plume interference control is not effective in the sense that the shock movement is insignificant. However, model PDE produces the plume-induced shock at a position of $x_s/D < 1$ and shifts it downstream by over 0.2 calibers for all conditions tested. For effective plume interference control with a porous extension, therefore, the location of the device must be chosen carefully.

For $p_c/p_a = 170.9$, Fig. 19 shows the effect of passive control on total drag with a change in the freestream Mach number. The total drag coefficient $C_D$ was evaluated for the missile surfaces including the nose, afterbody, and base of the missile models. At the freestream Mach numbers tested, the missile models have negative $C_D$ values. For the present missile configuration, which has a straight slender afterbody with a small base region, the base pressure is far higher than the ambient pressure at the given plume pressure ratio. This gives a negative component of the drag that dominates all other components, thus giving a negative drag coefficient. When compared with the simple missile model, model PW introduces an insignificant change in total drag. A slight drag reduction with the control method can be attributed to reduced shock strength (Figs. 11 and 12), consequently reducing wave drag. For model PDE, the use of the porous extension results in an increase in drag, but it is also insignificant. Therefore, the passive control methods employed for the present missile model are useful to improve the shock interactions at the tail fin location by moving the shock away from the fin or freezing the shock position with changes in flight conditions rather than by enhancing the performance in terms of drag reduction.

## Conclusions

An understanding of the physics of the plume-induced shock and separation was developed, particularly at high plume pressure ratios with and without shock–turbulent boundary-layer control methods, using CFD as a tool. Mass-averaged Navier–Stokes equations with the RNG $k$–$\varepsilon$ turbulence model were solved using a fully implicit finite volume scheme and time-marching algorithm. To characterize moderately to highly underexpanded plumes imbedded in supersonic flows, the plume pressure ratio was varied in the range of 50–350 at flight Mach numbers of 1.2–3.0.

For the model with a sharp edge, generally, an increase in the freestream Mach number introduced a stronger plume-induced shock and a reduced extent of shock interaction as the shock moved downstream. On the other hand, an increase in the plume pressure ratio led to an upstream movement of the shock with increased strength due to enlarged plume boundaries.

With a porous tail, when the plume-induced shock occurred near the control device, a self-circulation through the device produced a weaker shock and ensuing compression waves as leading compression instead of a single strong shock. Under such conditions, shock positions changed in a very small range and shock strength was considerably reduced. The effect of a porous extension attached at the missile base on shock interactions was mainly to restrain the plume from strongly underexpanding during a change in flight conditions. However, care needs to be taken for the design of a porous extension because of an adverse effect on the reduction of shock strength with an improper location of the device.

## References

[1] Albini, F. A., "Approximate Computation of Under-Expanded Jet Structure," *AIAA Journal*, Vol. 3, No. 8, 1965, p. 1538.

[2] Boynton, F. P., "Highly Under-Expanded Jet Structure: Exact and Approximate Calculations," *AIAA Journal*, Vol. 5, No. 9, 1967, pp. 1703–1704.

[3] Adamson, T. C., Jr., and Nicholls, J. A., "On the Structure of Jets from Highly Underexpanded Nozzles into Still Air," *Journal of the Aeronautical Sciences*, Vol. 26, No. 1, 1959, pp. 16–24.

[4] Alpinieri, L. J., and Adams, R. H., "Flow Separation Due to Jet Pluming," *AIAA Journal*, Vol. 4, No. 10, 1966, pp. 1865–1866.

[5] Fetterman, D. E., Jr., "Effects of Simulated Rocket-Jet Exhaust on Stability and Control of a Research-Type Airplane Configuration at a Mach Number of 6.86," NASA TM X-127, Oct. 1959.

[6] Yanowitch, S., and Hneuber, R. N., "Scout First Stage Flight Characteristics," NASA CR-111945, March 1968.

[7] Raghunathan, S., Kim, H. D., Benard, E., Mallon, P., and Harrison, R., "Plume Interference Effects on Missile Bodies," AIAA Paper 2001-0259, Jan. 2001.

[8] Salmi, R. J., "Effects of Jet Billowing on Stability of Missile-Type Bodies at Mach 3.85," NASA TN D-284, June 1960.

[9] Hinson, W. F., and McGhee, R. J., "Effects of Jet Pluming on the Static Stability of Five Rocket Models at Mach Number of 4, 5 and 6 and Static-Pressure Ratios up to 26,000," NASA TN D-4064, Aug. 1967.

[10] Hinson, W. F., and Falanga, R. A., "Effects of Jet Pluming on the Static Stability of Cone-Cylinder-Flare Configurations at Mach Number of 9.65," NASA TN D-1352, Sept. 1969.

[11] McGhee, R. J., "Some Effects of Jet Pluming on the Static Stability of Ballistics Bodies at a Mach Number of 6.00," NASA, TN D-3698, Nov. 1966.

[12] McGhee, R. J., and Martin, J. A., "Exploratory Investigation of Flow Field Resulting From Forward-Facing Nozzles Exhausting Near a Large Cylindrical Body at Free-Stream Mach Numbers of 3.0 to 6.0," NASA TN D-5030, March 1969.

[13] McGhee, R. J., "Jet-Plume-Induced Flow Separation on Axisymmetric Bodies at Mach Numbers of 3.00, 4.50 and 6.00," NASA TM X-2059, Aug. 1970.

[14] Wu, J. M., and Aoyama, K., "Pressure Distributions for Axisymmetric Bodies with Discontinuous Curvature in Transonic Flow," U.S. Army Missile Command, Technical Rept. RD-TR-70-25, Redstone Arsenal, AL, Nov. 1970.

[15] Wu, J. M., Aoyama, K., and Moulden, T. H., "Transonic Flow Field Calculation Around Ogive Cylinders by Non-linear-Linear Stretching Method," U.S. Army Missile Command, Technical Rept. RD-TR-70-12, Redstone Arsenal, AL, April 1970.

[16] Wu, J. M., Aoyama, K., and Moulden, T. H., "Transonic Flow Fields Around Various Bodies of Revolution Including Preliminary Studies on Viscous Effects With and Without Plume—Summary Report," U.S. Army Missile Command, Technical Rept. RD-TR-71-12, Redstone Arsenal, AL, May 1971.

[17] Matesanz, A., Velázquez, A., Perales, J. M., and Santiago-Prowald, J., "Numerical Simulation of Base-Flow/Plume Interaction," AIAA Paper 98-1597, April 1998.

[18] Bannink, W. J., Houtman, E. M., and Bakker, P. G., "Base Flow/Underexpanded Exhaust Plume Interaction in a Supersonic External Flow," AIAA Paper 98-1598, April 1998.

[19] Venkateswaran, S., Weiss, J. M., and Merkle, C. L., "Propulsion Related Flowfields Using the Preconditioned Navier–Stokes Equations," AIAA Paper 92-3437, July 1992.

[20] Yakhot, V., and Smith, L., "The Renormalization Group, the $\varepsilon$-Expansion and Derivation of Turbulence Models," *Journal of Scientific Computing*, Vol. 7, No. 1, 1992, pp. 35–61.

[21] *FLUENT 5 User's Guide*, Fluent, Inc., Lebanon, NH, 1998, Chap. 24.

[22] Barth, T. J., and Jespersen, D., "The Design and Application of Upwind Schemes on Unstructured Meshes," AIAA Paper 89-0366, Jan. 1989.

[23] Jameson, A., Schmidt, W., and Turkel, E., "Numerical Solution of the Euler Equations by Finite Volume Methods Using Runge–Kutta Time-Stepping Schemes," AIAA Paper 81-1259, June 1981.

[24] Burt, J. R., Jr., "An Experimental Investigation of the Effect of Several Rocket Plume Simulators on the Pressure Distribution of a Body of Revolution at Free Stream Mach Number of 0.9 to 1.2," U.S. Army Missile Command, Technical Rept. RD-TR-70-23, Redstone Arsenal, AL, Nov. 1970.

[25] Lee, Y. K., Raghunathan, S., Benard, E., Kim, H. D., and Setoguchi, T., "Effect of Rounded Afterbody on Plume Interference Around Slender Bodies," Confederation of European Aerospace Societies Aerospace Aerodynamics Research Conf., Paper-95, June 2002.

[26] Raghunathan, S., "Passive Control of Shock-Boundary Layer Interaction," *Progress in Aerospace Sciences*, Vol. 25, No. 3, 1988, pp. 271–296.

G. Candler
*Associate Editor*